

Modulated time evolution for efficient variational ground state preparation

Zekun He,^{1,*} A. F. Kemper,^{2,†} and J. K. Freericks^{1,‡}

¹*Department of Physics, Georgetown University, Washington DC 20057, USA*

²*Department of Physics, North Carolina State University, Raleigh, North Carolina 27695, USA*

(Dated: November 26, 2024)

Adiabatic state preparation aims to prepare the ground state of a target Hamiltonian starting from the easily prepared ground state of an initial Hamiltonian. While effective for time-dependent Hamiltonians with a significant energy gap to the first coupled excited state, this process becomes exceedingly slow as the gap becomes small. To accelerate it, we allow controlled diabatic excitations during the evolution and optimize the path to remove those excitations at the end of the evolution. This is done via a modulated time evolution (dynamically scaling the Hamiltonian) in addition to a field similar to the one used in local adiabatic time evolution, with the target to optimize the final energy of the unscaled Hamiltonian. This method is easy to implement and requires no complex counter-diabatic Hamiltonians and no prior knowledge of the system's energy gap. When the time evolution is further Trotterized, separating the spin-spin coupling terms and the magnetic-field terms into distinct factors, it becomes identical in structure to the quantum approximate optimization algorithm (QAOA). Compared to QAOA, the modulated time evolution often achieves the same level of performance with fewer layers (time steps).

I. INTRODUCTION

State preparation, especially ground state preparation, is a critically important algorithm for quantum computation. Adiabatic state preparation [1–3] (or more practically, finite-time evolution using the local adiabatic field [4, 5]), is a simple way to create the ground state, but it requires an extremely long time evolution for high fidelity, which ultimately makes it impractical. Shortcuts to adiabaticity [6–8] can prepare the ground state in significantly shorter time frames, but they usually require evolving the system with additional complicated counter-diabatic Hamiltonians [9–12], which are prohibitive to implement. To improve the feasibility of these methods, various approaches have been explored, such as variational-based counter-diabatic Hamiltonians [12, 13] and tensor network-based quantum circuit compression [14].

As we will show in this work, the key to accelerate adiabatic time evolution is being able to find a strategy that can return the amplitudes of diabatically excited states back to the ground state at the end of the time evolution, as shown in Fig. 1 panel (d). This is contrary to local adiabatic evolution, which is engineered solely to minimize the excitation out of the ground state, and does not optimize the possibility of returning weight back to the ground state (even if this often occurs). One way to separately engineer a return mechanism is to incorporate a variational principle into the time evolution. We do so by introducing a time-dependent scaling field $\tilde{\lambda}(t)$, which modulates the scale of the Hamiltonian $\tilde{\lambda}(t)\hat{H}_0(t)$ during the time evolution [see Eq. (1) for an example], and whose

temporal profile is chosen to minimize the energy of the final evolved state.

In this work, we examine the ground state preparation of the long-range transverse-field Ising model. We denote the initial Hamiltonian by \hat{H}_B (magnetic field term), and we write the (unmodulated) time-dependent Hamiltonian as $\hat{H}_0(t) = \hat{H}_A + B(t)\hat{H}_B$, such that the target Hamiltonian is $\hat{H}_0(t=t_f)$. In local adiabatic time evolution, which takes large time steps when the energy gap is large and small steps when it is small, one then constructs the most efficient control field, the locally adiabatic field, $B_{LA}(t)$, that engineers the same (small) diabatic excitation out of the ground state at each time step [4, 15]. One of the main issues with this method is that it requires *a priori* knowledge of the energy gap to the first coupled excited state, which is usually hard to obtain in practice for large or complex systems.

In modulated time evolution, we do not apply any *a priori* restrictions on the field $B(t)$ or the scaling factor $\lambda(t)$, allowing the system to create diabatic excitations as needed, and then removing them at the end, to minimize the energy. This is why this method does not require energy gap information. Our time-dependent Hamiltonian becomes

$$\hat{H}_{\text{mod}}(t) = \tilde{\lambda}(t) \left[\hat{H}_A + B(t)\hat{H}_B \right]. \quad (1)$$

In our calculations, the time-evolution operator is approximated by a Trotter product formula [16, 17], yielding a time-evolved state

$$|\psi_f\rangle = \prod_{j=1}^N e^{-i\hat{H}_{\text{mod}}(j\Delta t)} |\psi_0\rangle. \quad (2)$$

Since we use a variational principle to determine $\Delta t\tilde{\lambda}(t) =: \lambda(t)$, we simply absorb the time step Δt into the definition of the scale factor at a specific time.

* zh168@georgetown.edu

† akemper@ncsu.edu

‡ james.freericks@georgetown.edu

For optimization, the cost function is the final evolved energy, $E = \langle \psi_f | \hat{H}_0(t=t_f) | \psi_f \rangle$, with respect to the parameters $\lambda(t)$ and $B(t)$. We use a global optimization approach, meaning that we optimize both $\lambda(t)$ and $B(t)$ for all times at once, in contrast to optimizing them step by step or adaptively. This is because we aim to find a short trajectory that minimizes only the final evolved energy. By using global optimization, we can focus entirely on minimizing the final energy, rather than attempting to stay close to the instantaneous ground state throughout the evolution. In detail, we use gradient-based algorithms such as the BFGS algorithm [18, 19] or the ADAM algorithm [20]. One might be concerned about the high cost of global optimization. This is addressed in the Appendix A, where we show that for 8-site and 12-site systems, the number of iterations for convergence, given the same number of time steps, remains the same order of magnitude, even though the dimension of the matrix increases by a factor of 16. Hence, we have no evidence that the optimization becomes increasingly complex for larger system sizes, albeit, this is verified only for a few small systems.

The structure of this paper is as follows: First, we introduce the formalism of modulated time evolution. We then evaluate the performance of this approach across various scenarios, including (1) simplifying the time-dependent field, $\lambda(t)$, to a constant λ_0 , and (2) analyzing cases with varying energy gaps. Lastly, we present a numerical comparison of this method with the Quantum Approximate Optimization Algorithm (QAOA) [21, 22], demonstrating its superior performance relative to QAOA.

II. MODULATED TIME EVOLUTION

The long-range transverse-field Ising model is given by

$$\hat{H}_0(t) = \sum_{i < j} J_{i,j} \hat{\sigma}_z^{(i)} \hat{\sigma}_z^{(j)} + B(t) \sum_i \hat{\sigma}_x^{(i)}, \quad (3)$$

where we have $\hat{H}_A = \sum_{i < j} J_{i,j} \hat{\sigma}_z^{(i)} \hat{\sigma}_z^{(j)}$ and $\hat{H}_B = \sum_i \hat{\sigma}_x^{(i)}$. Here, $J_{i,j}$ are the Ising coupling strengths between spins at lattice sites i and j . In this study, we investigate cases such as long-range antiferromagnetic couplings, given by $J_{ij} = 1/|i - j|$, for $i \neq j$, as well as spin glass couplings, where the couplings J_{ij} are drawn independently from a Gaussian distribution: $J_{ij} \sim \mathcal{N}(\mu = 0, \sigma^2 = 1)$, with μ the mean and σ^2 the variance. This ensures that the couplings have zero mean and unit variance, providing a random disordered interaction for all i, j pairs.

The magnitude of the time-dependent transverse magnetic field is $B(t)$, and $\hat{\sigma}_\beta^{(i)}$ is the Pauli spin operator for spin i along the β direction. Most of our calculations are for 8-site and 12-site lattices, and we choose to prepare the ground state of Eq. (3) at $B(t_f) = 0.1$.

Given the total number of steps N , we propose initial guesses for the two fields, and the global optimization then determines $\lambda(t)$ and $B(t)$. For $B(t)$, since the energy gap is large when B is large and small when B is small, as an initial guess we ramp the initial B field down exponentially in the step number. In detail, the continuous field is given by: $B(t_j) = B_0 \exp(-j\tau/(N-1))$, where $\tau = \log(B_0/B_f)$, $B_0 = 1$, $B_f = 0.1$ and $j \in [0, N-1]$, with j being a positive integer.

For $\lambda(t)$, we use perturbation theory to help us determine what a reasonable initial guess is. We start our system in the ground state of the initial Hamiltonian \hat{H}_B , and then express the subsequent time evolution in the form

$$|\Psi(t)\rangle = \sum_n c_n(t) |n(t)\rangle e^{i\theta_n(t)}, \quad (4)$$

with the dynamical phase $\theta_n(t) = -\int_0^t \tilde{\lambda}(\bar{t}) E_n(\bar{t}) d\bar{t}$ and the instantaneous energy given by $\tilde{\lambda}(t) E_n(t)$; here, we have $\hat{H}_{\text{mod}}(t) |n(t)\rangle = \tilde{\lambda}(t) E_n(t) |n(t)\rangle$. The state at time t can be expanded in terms of the instantaneous eigenbasis, which forms a complete basis set.

The instantaneous state amplitude satisfies the differential equation

$$\begin{aligned} \frac{d}{dt} c_m(t) &= -c_m(t) \langle m(t) | \dot{m}(t) \rangle \\ &- \sum_{n \neq m} c_n(t) \frac{\tilde{\lambda}(t) \dot{B}(t) \langle m(t) | \hat{H}_B | n(t) \rangle}{\tilde{\lambda}(t) (E_n(t) - E_m(t))} e^{-i(\theta_n(t) - \theta_m(t))} \end{aligned} \quad (5)$$

The first term on the right-hand side is independent of $\tilde{\lambda}(t)$ because it depends solely on the eigenvectors and their changes. Unlike $B(t)$, which can affect the eigenvectors, $\tilde{\lambda}(t)$ does not influence them. Additionally, we note that the $\tilde{\lambda}(t)$ factors cancel out in the numerator and denominator of the second term, leaving its only dependence on the dynamical phase $\theta_n(t)$. For $\tilde{\lambda}(t)$ to significantly influence $c_m(t)$, the exponential phase factors must be on the order of 1. Based on this reasoning, our initial guess for $\lambda(t)$ is qualitatively chosen as a random array with values ranging from 1 to 2.

Most time evolution strategies [23–25] impose a constraint on the total time t_f used for the optimization. However, the total time t_f is not uniquely defined in modulated time evolution because we only know the product $\Delta t \tilde{\lambda}(t)$ without the ability to independently determine Δt . Instead, we focus on another equally important quantity: the total number of steps, N . In order to provide a brief comparison of modulated time evolution with adiabatic time evolution, it is convenient to use normalized time as the x -axis, as shown in Fig. 1, such that each modulated time evolution step is plotted with uniform spacing, calculated as the reciprocal of the total number of steps.

In Fig. 1 panel (a) and (b), we show the 46 steps optimized $\lambda(t)$ and $B(t)$ for the 12-site model. We can

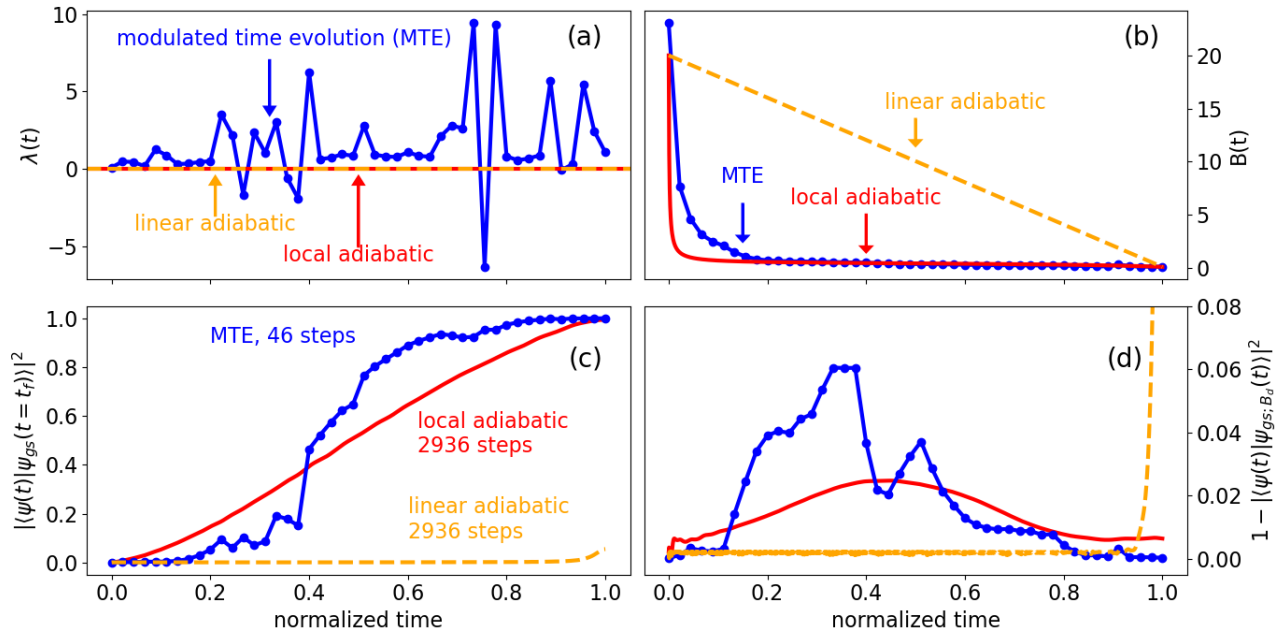


FIG. 1. Comparison of the modulated time evolution (represented by solid blue line with dots) with the adiabatic time evolution (local one represented by red solid line and linear one represented by orange dashed line) in the 12-site model, plotted in normalized time t/t_f . In modulated time evolution, t_f is not uniquely defined, so each step is plotted with uniform spacing, calculated as the reciprocal of the total number of steps. After a 50-step optimization procedure, steps where $\lambda(t)$ is smaller than 10^{-2} are removed, resulting in a total of 46 steps. In the local adiabatic evolution, the total time is 29.36 with the adiabaticity parameter $\rho = 10$, resulting in 2936 steps with $\Delta t = 0.01$ (see the Appendix B for more details on local adiabatic field). The same number of steps is then chosen for linear adiabatic evolution. (a) The optimized scaling parameter $\lambda(t)$. In the adiabatic evolution cases, the scaling factor $\tilde{\lambda}(t)$ is set to one with $\Delta t = 0.01$, resulting in $\lambda(t) = 0.01$. (b) The optimized field $B(t)$. (c) Target ground state fidelity at each step of the evolution. Note that linear adiabatic evolution performs poorly as it does not slow down when the energy gap is small, where most diabatic excitation occurs. (d) The instantaneous diabatic excitation, quantified as an infidelity.

see that the optimized $\lambda(t)$ exhibit oscillations centered about 1 in this case. Across the different number of steps, there is no clear pattern regarding the frequency or amplitude of these oscillations, suggesting that they are instead optimized with respect to the total number of steps and the initial guess, rather than being governed by some physical energy scale in the system. In contrast, the shape of $B(t)$ converges to a shape reminiscent of the local adiabatic field (see the the Appendix B), when it is plotted on a normalized time axis corresponding to the number of steps.

In Fig. 1, panel (d), we present the instantaneous diabatic excitation as a function of normalized time, comparing it to the adiabatic evolution. This plot highlights how the modulated time evolution enables the evolved state to deviate from the instantaneous ground state while ultimately eliminating diabatic excitations to achieve a high target ground state fidelity.

The definition of instantaneous ground state fidelity used here differs from the conventional approach. At each time step, we identify the B value that yields the highest instantaneous ground state fidelity and use that B value to determine the instantaneous ground state, which we denote as $B_d(t)$. These values are also shown in Fig. 2

for the three cases used in Fig. 1. This approach is necessary because, now that optimization is applied to the $B(t)$ field, the optimized $B(t)$ may not decrease monotonically or approach the instantaneous target B value quickly enough. For instance, if the instantaneous target B value is 0.2, but the applied B field remains at 0.6, the system may exhibit an increased level of instantaneous excitation. Thus, using the standard method (i.e., directly relying on the $B(t)$ field) for defining the instantaneous ground state may not provide sufficient accuracy. By adopting this approach, we calculate an infidelity with the best ground state determined over all possible B values, which represents the minimum possible diabatic excitation the system can have. Consequently, Fig. 1, panel (d), clearly demonstrates that modulated time evolution deviates the system from the instantaneous ground state, creating diabatic excitations but successfully eliminating them by the end, achieving high target ground state fidelity.

Additionally, in the case of local adiabatic evolution shown in panel (d), there is also a return in the instantaneous ground state fidelity. However, this is attributed to finite-time evolution effects, as true adiabatic evolution—under infinitely slow processes—would result

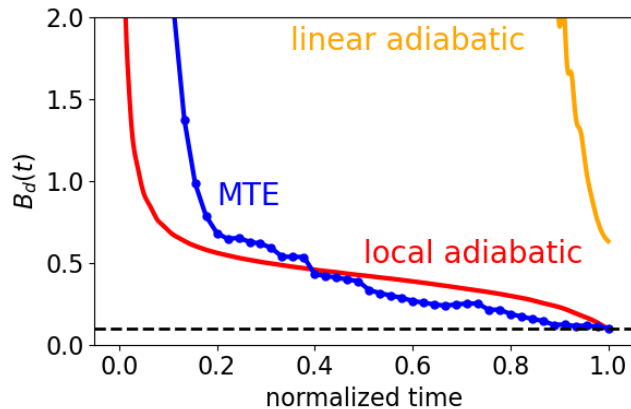


FIG. 2. The $B_d(t)$ field associated with the three cases in Fig. 1, with the black horizontal dashed line indicating the target $B = B(t = t_f) = 0.1$. This plot also helps to explain why the linear adiabatic approach performs poorly: it spends most of the evolution time before the critical B value, which is approximately 0.42 in this case. As a result, the final evolved state remains barely close to the instantaneous ground state around $B \approx 0.6$, staying in the paramagnetic phase rather than transitioning to the antiferromagnetic phase after the critical point. This behavior leads to a low target ground state fidelity, as shown in Fig. 1, panel (c).

in a flat line at 1. More details are provided in the Appendix C, which demonstrates that the return amplitude of the instantaneous ground state fidelity can be significantly reduced by adopting a more adiabatic-like evolution setting. Interestingly, similar returning behavior was also observed in [26], which studied the dependence of Trotter error on total evolution time and time-step size.

A. Constant λ_0 time evolution

As we saw in the previous section, there is no clear pattern in the optimized $\lambda(t)$. This flexibility provides the freedom to restrict the shape of $\lambda(t)$ to fit feasible analog quantum simulation experimental settings.

Currently, the optimization is not restricted for $\lambda(t)$, but for practical reasons, one might impose a bounded range for $\lambda(t)$ or other specific settings. To demonstrate that this does not significantly affect modulated time evolution, aside from potentially requiring more steps, we present the most extreme case: reducing $\lambda(t)$ to a single parameter, $\lambda(t) = \lambda_0$.

In Fig. 3, we present results using a single constant parameter λ_0 . The data is displayed as a heatmap showing the target ground state infidelity across varying values of λ_0 and the number of steps, with no optimization of $B(t)$ needed; $B(t)$ is set as an exponentially decreasing field with $B_0 = 10$. With only a single parameter to optimize, a wide range of λ_0 and step count combina-

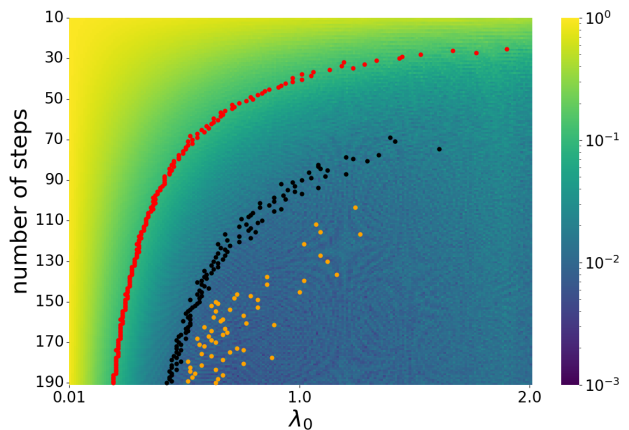


FIG. 3. Infidelity heatmap of a constant λ_0 -modulated time evolution for an 8-site model. For each step count, the dots highlights the minimum λ_0 values required to reach specific infidelity thresholds: 0.1 (red), 0.01 (black), and 0.005 (orange).

tions yield fidelities of at least 0.99, though the highest fidelity we achieved was only 0.997. By contrast, modulated time evolution achieves 0.99 fidelity with an order of magnitude fewer steps.

In Fig. 4, the instantaneous ground state fidelity at different $B_d(t)$ values are shown, plotted with the step of index as the x-axis. This plot aligns with the behavior observed in modulated time evolution, demonstrating a return in instantaneous ground state fidelity. In particular, this case primarily introduces diabatic excitations around the critical B value, followed by a return to the instantaneous ground state, which coincides with the target ground state at the final time.

B. Energy gap dependence

In adiabatic evolution, it is well established that the total evolution time scales as $\propto 1/\Delta^2$, where Δ represents the minimum energy difference between the ground state and the first coupled excited state during the evolution [4]. As the system size increases, systems that become gapless at the critical point in the thermodynamic limit experience a continual decrease in the energy gap, posing significant challenges for adiabatic time evolution in large systems with narrow energy gaps. Hence, it is of particular interest to explore how modulated time evolution performs as the system size increases and the energy gap narrows.

Unlike the quantum Monte Carlo method [27], which can simulate systems with hundreds of spins, the classical simulation currently employed relies on the matrix exponential of the time evolution operator. The time complexity of this approach scales as $O(n^3)$ [28] for a general dense matrix, where n is the dimension of the matrix

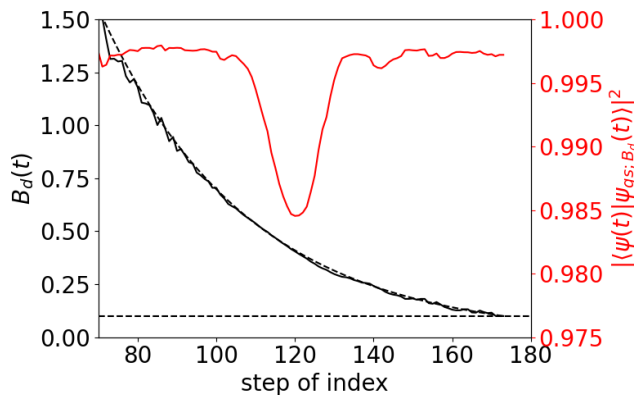


FIG. 4. The $B_d(t)$ and instantaneous ground state fidelity are plotted as a function of the step of index, using the best parameter set found in Fig. 3, with $\lambda_0 = 0.67$ and 174 steps. The $B_d(t)$ is shown in black, while a black dashed line represents the applied $B(t)$ field. The instantaneous ground state fidelity is depicted in red, showing a visible drop and subsequent return around $B \approx 0.42$, which corresponds to the critical B value in this system. This plot starts at a step index of 70 because little activity occurs before this point, as the instantaneous ground state fidelity remains close to 1 there.

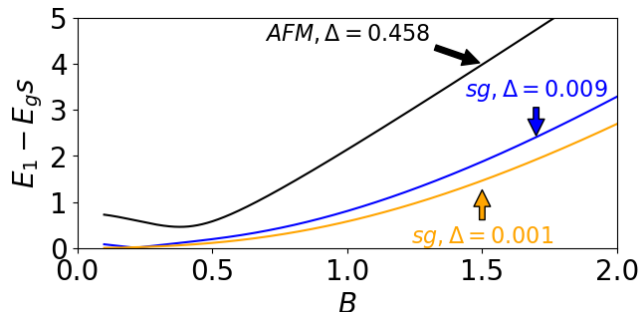


FIG. 5. Energy gap between the first coupled excited state and the ground state for the antiferromagnetic (AFM) system and two different spin glass (sg) systems calculated on an 8-site lattice.

in Eq. (2). As a result, the simulation is restricted to small lattice sizes, preventing scaling analysis for larger systems. Instead, we focus on spin-glass systems with substantially smaller energy gaps to emphasize the weak energy gap dependence of this method.

We focus on an 8-site system, generating various energy gap scenarios using a spin-glass model, as shown in Fig. 5. We investigate the dependence of the number of steps, N , on the energy gap. By varying the energy gaps in this controlled setup, we observe that even when the energy gap decreases by a factor of over 100, as opposed to the time requirement increasing by approximately 100^2 , as predicted by adiabatic scaling, modu-

lated time evolution requires only 3 to 4 times more time steps to achieve the same energy ratio accuracy, as shown in Table I.

steps	AFM	spin glass	
	$B_c = 0.38$ $\Delta = 0.458$	$B_c = 0.215$ $\Delta = 0.009$	$B_c = 0.1$ $\Delta = 0.001$
10	3.55×10^{-3}	5.05×10^{-2}	5.33×10^{-2}
20	2.67×10^{-4}	3.08×10^{-2}	1.79×10^{-2}
50	3.04×10^{-5}	1.58×10^{-2}	1.19×10^{-2}
80	5.57×10^{-10}	7.15×10^{-3}	2.69×10^{-3}
200	\	9.22×10^{-10}	1.67×10^{-8}
300	\	\	3.35×10^{-10}

TABLE I. $1 - E/E_{gs}$ results for the 8-site model, where E is the final evolved energy.

steps	AFM	spin glass	
	$B_c = 0.38$ $\Delta = 0.458$	$B_c = 0.215$ $\Delta = 0.009$	$B_c = 0.1$ $\Delta = 0.001$
10	9.28×10^{-3}	7.79×10^{-1}	1.61×10^{-1}
20	3.97×10^{-4}	7.18×10^{-1}	6.14×10^{-2}
50	3.20×10^{-5}	9.63×10^{-1}	7.04×10^{-2}
80	5.86×10^{-10}	3.31×10^{-1}	1.69×10^{-2}
200	\	9.00×10^{-9}	2.23×10^{-4}
300	\	\	3.28×10^{-7}

TABLE II. Target ground state infidelity results for the 8-site model.

III. CONNECTION AND COMPARISON TO QAOA

In the previous section, we provided a comparison between modulated time evolution and adiabatic time evolution to highlight the differences in their evolution dynamics: one can introduce but later remove diabatic excitations, while the other is engineered to only avoid them (even if it removes some anyway). However, for efficiency, this is not a fair comparison between the two. While modulated time evolution is efficient in terms of the number of time steps, it requires many energy measurements, which adiabatic time evolution does not, and it also involves an additional control field, $\lambda(t)$. Therefore, it is more appropriate to compare the performance of modulated time evolution with the QAOA, as both methods can have the same number of parameters and rely on the variational principle.

The quantum approximate optimization algorithm [21, 22] is a simple to implement yet powerful protocol [29–31], which involves p layers, with each layer corresponding to the application of a mixing Hamiltonian \hat{H}_B (weighted by the angle β_j) and a problem Hamiltonian \hat{H}_A (weighted by the angle γ_j), with j denoting the layer (from 1 to p). The QAOA then has the following varia-

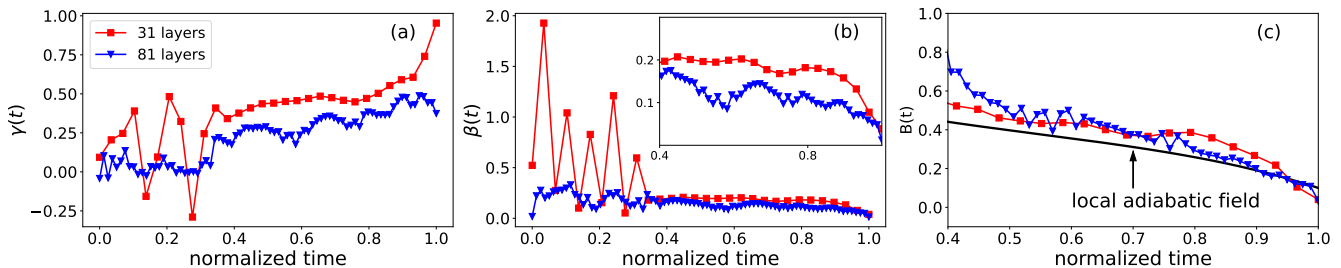


FIG. 6. Optimized 8-site QAOA angles and its ratio versus normalized time. (a) QAOA angle $\gamma(t)$. (b) QAOA angle $\beta(t)$. (c) The ratio $\beta(t)/\gamma(t)$. The ratio compares with the locally adiabatic field, which is plotted in the black solid line. Note, we count the last single term $\exp\{-i\gamma\hat{H}_A/(2m)\}$ as one layer, resulting in the total number of layers to be 31 and 81.

tional ansatz for the optimization problem:

$$|\psi_f\rangle = e^{-i\beta_p\hat{H}_B} e^{-i\gamma_p\hat{H}_A} e^{-i\beta_{p-1}\hat{H}_B} e^{-i\gamma_{p-1}\hat{H}_A} \dots \\ \times e^{-i\beta_1\hat{H}_B} e^{-i\gamma_1\hat{H}_A} |\psi_0\rangle, \quad (6)$$

which constructs the final ansatz state $|\psi_f\rangle$ in terms of the initial state $|\psi_0\rangle$. The initial state $|\psi_0\rangle$ is also the ground state of \hat{H}_B . Note that the main difference from modulated time evolution is that QAOA does not put the full Hamiltonian into one exponent in each layer (time step), but instead breaks it up into the application of the problem and mixing Hamiltonians separately.

Many studies have been performed to understand and improve QAOA [32–41], link QAOA to optimal control theory [23, 42, 43], or the counter-diabatic method [44–46] in an effort to reveal the underlying nature of QAOA angles, with the aim of finding a more efficient strategy to optimize the angles.

In this work, to obtain the QAOA angles, we begin by rewriting the modulated time evolution expression in Eq. (2) into the QAOA form, as in Eq. (6). Specifically, we employ a second-order Trotter product formula to transform a single layer from our previous calculations into m layers in the QAOA expression, as follows:

$$e^{-i(\lambda\hat{H}_A + \lambda B\hat{H}_B)} = e^{-i\frac{\lambda}{2m}\hat{H}_A} \left(e^{-i\frac{\lambda}{m}\hat{H}_A} e^{-i\frac{\lambda B}{m}\hat{H}_B} \right)^m \\ \times e^{-i\frac{\lambda}{2m}\hat{H}_A} + O\left(\frac{1}{m^2}\right). \quad (7)$$

This Trotter formula translates the modulated time evolution form into the QAOA form. For each time step in the modulated time evolution, we select a separate number of Trotter terms, m , such that the final energy from the QAOA form remains within 30% of the energy obtained from the modulated time evolution form. The 30% margin is chosen empirically: if the margin is too narrow, it results in an excessive number of layers in the QAOA form. Conversely, if the margin is too wide, the energy from the QAOA form deviates significantly from the pre-Trotter result, making the resulting angles unhelpful, as arbitrary angles could potentially produce

similar energy values. This process typically maps the number of layers from N in modulated time evolution to approximately $4N$ in QAOA. More details are provided in the Appendix D.

The second step is to use the Trotterization angles as an initial guess for QAOA optimization. This improved initial guess often results in much better QAOA angles compared to using an uninformed initial guess. In Ref. [29], QAOA angles are optimized for up to 30 layers, achieving a final target ground state fidelity close to 0.999. Here, for the exact same case, we test the higher limits of QAOA using the optimization approach described above, demonstrating that QAOA can achieve significantly higher accuracy if we allow for more layers, with infidelity on the order of 10^{-8} , as shown in Fig. 7.

To explore the connection between modulated time evolution and QAOA, we plot QAOA angles for different numbers of layers for the 8-site model in Fig. 6. Upon examining QAOA angles across various layer counts and system sizes, a trend emerges: the late-time ratio of $\beta(t)/\gamma(t)$ agrees with the local adiabatic field. Significant spikes in both angles, $\beta(t)$ and $\gamma(t)$, can occur initially, but most data points eventually converge closer to the local adiabatic field. This observation is supported not only by the QAOA angles found in this work but also by the QAOA angles reported in Ref. [29], which employs a completely different optimization scheme.

If we instead start with the QAOA expression and rewrite it into a single exponential form, we obtain

$$e^{i\gamma(t)\hat{H}_A} e^{i\beta(t)\hat{H}_B} \approx e^{i\gamma(t)(\hat{H}_A + \frac{\beta(t)}{\gamma(t)}\hat{H}_B - \frac{i\beta(t)}{2}[\hat{H}_A, \hat{H}_B] + \dots)}. \quad (8)$$

from the Baker-Campbell-Hausdorff formula truncated to the lowest-order correction. Focusing on the dominant terms, $\gamma(t)$ and $\beta(t)/\gamma(t)$ (since most QAOA angles are on the order of 10^{-1} , making higher-order terms negligible), we interpret $\gamma(t)$ as a prefactor and $\beta(t)/\gamma(t)$ as a time-dependent field, analogous to $\lambda(t)$ and $B(t)$ in modulated time evolution. The similarity between $\beta(t)/\gamma(t)$ in QAOA and $B(t)$ in modulated time evolution, underscores a connection between the two methods. Both rely on an approximate locally adiabatic field to guide transitions between magnetic field values in the Hamiltonian,

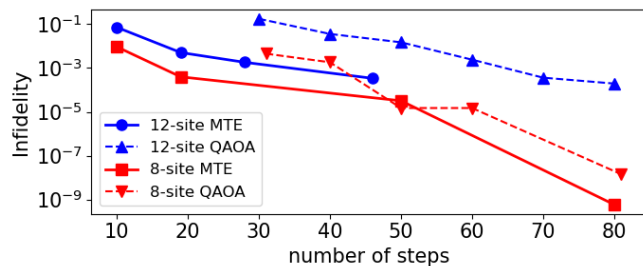


FIG. 7. Target ground state infidelity versus number of steps from using modulated time evolution and QAOA in 8-site and 12-site model. It is important to note that for the 12-site calculations presented here, we stopped at 80 steps due to computational limitations, not because of performance convergence.

with $\gamma(t)$ and $\lambda(t)$ optimized to minimize the final energy, respectively.

In Fig. 7, it shows the target ground state infidelity for both 8-site and 12-site models as a function of the number of steps, using both modulated time evolution and QAOA. This leads to a significant observation: modulated time evolution represents a more effective approach for state preparation compared to QAOA, as it typically requires about half the number of steps needed by QAOA to achieve the same performance. While this conclusion is currently supported only by numerical results, it raises an intriguing question for future research: how can this be understood analytically in terms of the additional higher-order commutators? Some progress has already been made in exploring these commutators for counter-diabatic purposes [44]. However, incorporating the return mechanism philosophy could provide a fresh perspective to revisit this topic.

IV. CONCLUSION

In this work, we find that modulated time evolution can be a valuable approach for finding the ground state. Investigating its robustness against noise and potential hardware limitations will provide additional insights into

its practical application.

Modulated time evolution also offers an alternative perspective for studying the quantum speed limit. Traditionally, quantum speed limit studies focus on determining the minimum time required to evolve one state into another. In Ref. [47], it is shown that using the trace norm of an auxiliary counter-diabatic Hamiltonian as a measure of implementation complexity for shortcuts to adiabaticity reveals a fundamental trade-off between speed and cost: the faster a quantum system evolves along its adiabatic manifold, the higher the cost of implementing the shortcut. In contrast, modulated time evolution approaches this from the opposite end, aiming to minimize complexity and reduce the number of steps required. Instead of introducing auxiliary terms or relying on knowledge of the energy gap, this approach addresses the question of how to modulate the original system Hamiltonian, based solely on energy measurements, to achieve optimal evolution in a minimum number of steps. The strength of modulated time evolution lies in its ability to control diabatic excitations. We numerically demonstrate the return mechanism, though the fundamental criteria for this mechanism remain an open question that we hope will be examined soon.

V. ACKNOWLEDGMENT

We thank Aniruddha Bapat and Alexey Gorshkov for providing the QAOA data from Ref. [29]. We acknowledge helpful discussions with Shuchen Zhu about Trotter product formula errors and Efekan Kökcü about time evolution in spin models. This work was supported by the Department of Energy, Office of Basic Energy Sciences, Division of Materials Sciences and Engineering under grant no. DE-SC0023231. J.K.F. was also supported by the McDevitt bequest at Georgetown.

VI. DATA AVAILABILITY

The data that support the findings of this article as well as the python code that run the calculations are openly available at [48].

[1] M. Born and V. Fock, *Z. Phys.* **51**, 165 (1928).
 [2] S. Jansen, M.-B. Ruskai, and R. Seiler, *J. Math. Phys.* **48**, 102111 (2007).
 [3] E. Farhi, J. Goldstone, S. Gutmann, and M. Sipser, arXiv <https://doi.org/10.48550/arXiv.quant-ph/0001106> (2000).
 [4] J. Roland and N. J. Cerf, *Phys. Rev. A* **65**, 042308 (2002).
 [5] P. Richerme, C. Senko, J. Smith, A. Lee, S. Korenblit, and C. Monroe, *Phys. Rev. A* **88**, 012334 (2013).

[6] D. Guéry-Odelin, A. Ruschhaupt, A. Kiely, E. Torrontegui, S. Martínez-Garaot, and J. G. Muga, *Rev. Mod. Phys.* **91**, 045001 (2019).
 [7] N. N. Hegade, K. Paul, Y. Ding, M. Sanz, F. Albarrán-Arriagada, E. Solano, and X. Chen, *Phys. Rev. Appl.* **15**, 024038 (2021).
 [8] K. Wan and I. Kim, arXiv <https://doi.org/10.48550/arXiv.2004.04164> (2004).

- [9] M. Demiralp and S. A. Rice, *J. Phys. Chem. A* **107**, 9937 (2003).
- [10] M. Demiralp and S. A. Rice, *J. Phys. Chem. B* **109**, 6838 (2005).
- [11] M. V. Berry, *J. Phys. A: Math. Theor.* **42**, 365303 (2009).
- [12] I. Čepaitė, A. Polkovnikov, A. J. Daley, and C. W. Duncan, *PRX Quantum* **4**, 010312 (2023).
- [13] C. Li, J. Shen, R. Shaydulin, and M. Pistoia, arXiv <https://doi.org/10.48550/arXiv.2403.01854> (2024).
- [14] C. Mc Keever and M. Lubasch, *PRX Quantum* **5**, 020362 (2024).
- [15] A. Francis, E. Zelleke, Z. Zhang, A. F. Kemper, and J. K. Freericks, *Symmetry* **14**, 809 (2022).
- [16] H. F. Trotter, *Proc. Amer. Math. Soc.* **10**, 545 (1959).
- [17] M. Suzuki, *J. Math. Phys.* **32**, 400 (1991).
- [18] P. Virtanen, R. Gommers, T. E. Oliphant, M. Haberland, T. Reddy, D. Cournapeau, E. Burovski, P. Peterson, W. Weckesser, J. Bright, S. J. van der Walt, M. Brett, J. Wilson, K. J. Millman, N. Mayorov, A. R. J. Nelson, E. Jones, R. Kern, E. Larson, C. J. Carey, Í. Polat, Y. Feng, E. W. Moore, J. VanderPlas, D. Laxalde, J. Perktold, R. Cimrman, I. Henriksen, E. A. Quintero, C. R. Harris, A. M. Archibald, A. H. Ribeiro, F. Pedregosa, P. van Mulbregt, and SciPy 1.0 Contributors, *Nat. Methods* **17**, 261 (2020).
- [19] M. Blondel, Q. Berthet, M. Cuturi, R. Frostig, S. Hoyer, F. Llinares-López, F. Pedregosa, and J.-P. Vert, arXiv [arXiv:2105.15183](https://arxiv.org/abs/2105.15183) (2021).
- [20] A. Paszke, S. Gross, S. Chintala, G. Chanan, E. Yang, Z. DeVito, Z. Lin, A. Desmaison, L. Antiga, and A. Lerer, (2017).
- [21] E. Farhi, J. Goldstone, and S. Gutmann, arXiv <https://doi.org/10.48550/arXiv.1411.4028> (2014).
- [22] E. Farhi and A. W. Harrow, arXiv <https://doi.org/10.48550/arXiv.1602.07674> (2016).
- [23] L. T. Brady, C. L. Baldwin, A. Bapat, Y. Kharkov, and A. V. Gorshkov, *Phys. Rev. Lett.* **126**, 070505 (2021).
- [24] F. Petziol, B. Dive, F. Mintert, and S. Wimberger, *Phys. Rev. A* **98**, 043436 (2018).
- [25] M. Bukov, A. G. R. Day, D. Sels, P. Weinberg, A. Polkovnikov, and P. Mehta, *Phys. Rev. X* **8**, 031086 (2018).
- [26] L. K. Kovalsky, F. A. Calderon-Vargas, M. D. Grace, A. B. Magann, J. B. Larsen, A. D. Baczewski, and M. Sarovar, *Phys. Rev. Lett.* **131**, 060602 (2023).
- [27] M. P. Kaicher, D. Vodola, and S. B. Jäger, *Phys. Rev. B* **107**, 165144 (2023).
- [28] N. J. Higham, *SIAM Journal on Matrix Analysis and Applications* **26**, 1179 (2005).
- [29] G. Pagano, A. Bapat, P. Becker, K. S. Collins, A. De, P. W. Hess, H. B. Kaplan, A. Kyprianidis, W. L. Tan, C. Baldwin, L. T. Brady, A. Deshpande, F. Liu, S. Jordan, A. V. Gorshkov, and C. Monroe, *Proc. Nat. Acad. Sci. (USA)* **117**, 25396 (2020).
- [30] R. Shaydulin, C. Li, S. Chakrabarti, M. DeCross, D. Herman, N. Kumar, J. Larson, D. Lykov, P. Minssen, Y. Sun, *et al.*, arXiv <https://doi.org/10.48550/arXiv.2308.02342> (2023).
- [31] P. C. Lotshaw, G. Siopsis, J. Ostrowski, R. Herrman, R. Alam, S. Powers, and T. S. Humble, *Phys. Rev. A* **108**, 042411 (2023).
- [32] V. Kremenetski, A. Apte, T. Hogg, S. Hadfield, and N. Tubman, arXiv <https://doi.org/10.48550/arXiv.2305.04455> (2023).
- [33] J. Kim, J. Kim, and D. Rosa, *Phys. Rev. Res.* **3**, 023203 (2021).
- [34] P. C. Lotshaw, T. S. Humble, R. Herrman, J. Ostrowski, and G. Siopsis, *Quantum Inf. Process* **20**, 403 (2021).
- [35] M. Streif and M. Leib, arXiv e-prints <https://doi.org/10.48550/arXiv.1901.01903> (2019).
- [36] S. H. Sack and M. Serbyn, *quantum* **5**, 491 (2021).
- [37] P. Díez-Valle, D. Porrás, and J. J. García-Ripoll, *Phys. Rev. Lett.* **130**, 050601 (2023).
- [38] P. Vikstål, M. Grönkvist, M. Svensson, M. Andersson, G. Johansson, and G. Ferrini, *Phys. Rev. Applied* **14**, 034009 (2020).
- [39] D. Willsch, M. Willsch, F. Jin, K. Michielsen, and H. De Raedt, *Comput. Phys. Commun.* **278**, 108411 (2022).
- [40] T. Lubinski, C. Coffrin, C. McGeoch, P. Sathe, J. Apanavicius, and D. E. B. Neira, arXiv <https://doi.org/10.48550/arXiv.2302.02278> (2023).
- [41] J. Yao, H. Li, M. Bukov, L. Lin, and L. Ying, in *Proceedings of Mathematical and Scientific Machine Learning*, Proceedings of Machine Learning Research, Vol. 190, edited by B. Dong, Q. Li, L. Wang, and Z.-Q. J. Xu (PMLR, 2022) pp. 49–64.
- [42] L. Kocia, L. Brady, P. Bienias, A. Bapat, and A. Gorshkov, *Behavior of Analog Quantum Algorithms*, Tech. Rep. SAND2021-3375C (Sandia National Lab, 2021).
- [43] D. An and L. Lin, *ACM TQC* **3**, 1 (2022).
- [44] J. Wurtz and P. J. Love, *Quantum* **6**, 635 (2022).
- [45] J. Wurtz and P. Love, *Phys. Rev. A* **103**, 042612 (2021).
- [46] P. Chandarana, N. N. Hegade, K. Paul, F. Albarrán-Arriagada, E. Solano, A. Del Campo, and X. Chen, *Phys. Rev. Res.* **4**, 013141 (2022).
- [47] S. Deffner and S. Campbell, *J. Phys. A: Math. Theor.* **50**, 453001 (2017).
- [48] J. K. F. Z. He, A. F. Kemper, *Dataset* (2024).
- [49] P. F. Velleman and D. C. Hoaglin, *Applications, basics, and computing of exploratory data analysis* (Duxbury Press, 1981).
- [50] Google, *Jax: Autograd and xla* (2018), software available from <https://github.com/google/jax>.
- [51] A. M. Childs, Y. Su, M. C. Tran, N. Wiebe, and S. Zhu, *Phys. Rev. X* **11**, 011020 (2021).
- [52] C. Yi and E. Crosson, *Npj Quantum Inf.* **8**, 37 (2022).

Appendix A: Numerics for the optimization process

In this study, we implement optimization procedures using two optimizers and compilation techniques tailored to the computational resources.

1. 8-site model

We use the BFGS optimizer from the SciPy package [18]. This implementation provides information on both the number of iterations and the total number of evaluations of the objective function (energy measurements in our case), including the energy measurements needed to obtain the gradient using the finite difference approximation method. And the convergence criterion we use is the L2 norm of the gradient being smaller than 10^{-5} .

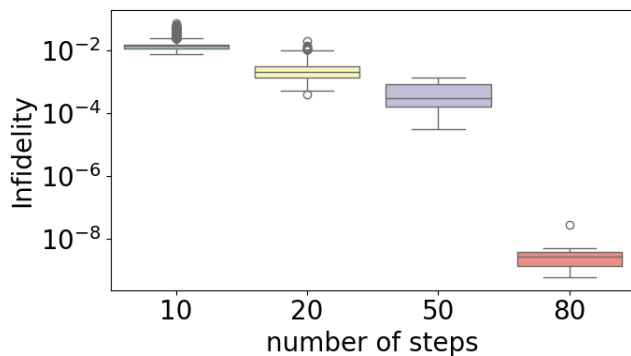


FIG. A1. Box plot of the fidelity versus the number of steps for the 8-site model. The number of runs for 10, 20, 50, and 80 layers are 6813 (6418) total (successful), 469 (360), 25 (21), and 22 (22), respectively.

In Fig. A1, we present a boxplot[49] of the 8-site optimization results, illustrating the convergence performance with various initial guesses over different numbers of steps. The initial guess for $\lambda(t)$ is an array with random values ranging from 1 to 2.

In the boxplot, the line inside the box represents the median. The lower edge is the first quartile, the median of the lower half (25th percentile). The upper edge is the third quartile, the median of the upper half (75th percentile). Whiskers extend to the smallest and largest values within 1.5 times of the interquartile range. Points outside this range are outliers, shown as individual circles.

From this plot, it is evident that the fidelity is fairly consistent across different initial guesses, indicating that the optimization process does not heavily depend on the initial guess. Approximately 20% (or less) of the runs fail to converge due to the inability of the optimizer to continue to successfully approximate the gradient. Even for failed cases, the final optimization results are usually pretty good, but we do not include them in the boxplots.

In Fig. A2, we present a boxplot showing the number of iterations versus fidelity in a 20-step optimization, using data from the 6418 convergence cases (out of 6813 tries). The number of iterations refers to how many times the optimizer updates λ and B . The plot reveals that even though the optimizer sometimes requires significantly more iterations to converge, the median fidelity remains fairly consistent. This suggests the existence of many different local minima with similar energy levels but varying difficulties in finding them. Overall, it takes a few 100's of iterations to complete the optimization. In this case, it requires about 10 energy measurements per iteration.

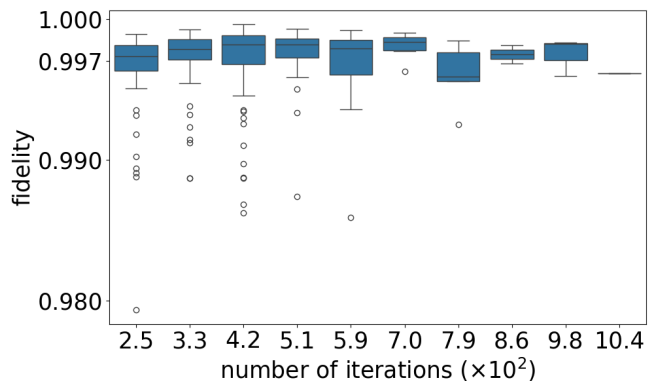


FIG. A2. Box plot for the 8-site model with 20 steps. We only include cases that successfully converged. The plot shows the number of iterations versus converged fidelity.

2. 12-site model

For modulated time evolution optimization, we employ the BFGS optimizer with automatic differentiation, using the JAX python package [19, 50] with GPU support. Due to the use of automatic differentiation, the number of energy measurements is significantly reduced. We report the number of iterations needed for the modulated time evolution optimization: 183 for 10 layers, 267 for 20 layers, 450 for 30 layers, and 2452 for 50 layers. These results are comparable to those obtained from the 8-site model, indicating good scalability to larger systems.

However, this efficient implementation relies on constructing a computational graph, which results in higher memory requirements for QAOA optimization compared to modulated time evolution optimization for the same number of parameters. Due to memory limitations on our hardware, we use the Adam optimizer in PyTorch [20].

The Adam optimizer with its built-in momentum feature, is designed to escape local minima. Thus, setting a threshold for the norm of the gradient or the change in the cost function may lead to early termination without achieving a successful outcome, because the optimal result is often one that does not have the smallest gradient norm. Instead, we set a maximum number of iterations and, once completed, select the best result found during the process. In this work, we empirically set the maximum number of iterations to be 20000.

Appendix B: local adiabatic field construction and its comparison to the optimal $B(t)$

The local adiabatic ramp is chosen in such a way that the diabatic excitation out of the ground state is uniform for each time interval [4, 5]. The Landau-Zener problem tells us that the diabatic excitation depends on the instantaneous energy gap between the ground state and

the first excited state of the same symmetry. We call this energy gap $\Delta(B(t))$, or more simply $\Delta(B)$.

Because the solution to the Landau-Zener problem tells us that the ratio of the square of the gap to the rate which we evolve the Hamiltonian determines the diabatic excitation, we define an adiabaticity parameter ρ , by

$$\rho = \left| \frac{\Delta^2(B)}{\dot{B}(t)} \right| \quad (\text{B1})$$

and the local adiabatic field is determined by the function $B(t)$ that keeps ρ constant over each time interval. This gives us

$$t = \int_0^t d\bar{t} = \rho \int_{B_0}^B \frac{1}{\Delta^2(\bar{B})} d\bar{B}, \quad (\text{B2})$$

where we must pick the initial and current magnetic fields to determine the current time. By stepping the current magnetic field, we use the integral to generate the profile $t(B)$ (which is a monotonic increasing function) and then invert it to find the local adiabatic field $B(t)$ for the evolution to the final time t_f (determined by the integral with an upper limit of B_{end}) and the adiabaticity parameter. An example for 12-site transverse field Ising model with $J_{ij} = 1/|i-j|^{-1}$ for $i \neq j$ is shown in Fig. B1.

The instantaneous gap $\Delta(B)$ is calculated in the symmetry sector of the ground state by an exact diagonalization calculation. There are two parity symmetries for the transverse-field Ising model—a spin reflection parity and a spatial inversion parity. The spin-reflection parity is the eigenvalue of the ground state with respect to the spin-reflection operator, which takes $\sigma_x^{(i)} \rightarrow \sigma_x^{(i)}$, $\sigma_y^{(i)} \rightarrow -\sigma_y^{(i)}$, and $\sigma_z^{(i)} \rightarrow -\sigma_z^{(i)}$. The second symmetry is a spatial inversion symmetry. If we have N lattice sites (with $i = 1, 2, \dots, N$), then the transformation $i \rightarrow N+1-i$ is a symmetry of the Hamiltonian because $J_{N+1-i, N+1-j} = J_{i,j}$. For 8(12)-sites and the antiferromagnetic case, the ground state is in the even-even sector. This reduces the Hamiltonian size from a dimension 256(4096) matrix to a dimension 72(1056) matrix and it allows us to easily identify the energy gap to the state with the same symmetry sector.

In Fig. B2, the optimal $B(t)$ with different numbers of steps is plotted along with the local adiabatic field on a normalized time axis. It is suggestive that the optimal $B(t)$ resembles the local adiabatic field more and more as the number of steps increases.

Appendix C: Instantaneous fidelity versus $B(t)$ in adiabatic time evolution

We present additional details on the instantaneous ground state fidelity throughout the local adiabatic process, using the magnetic field $B(t)$ as the x -axis instead of the normalized time axis discussed in the main text.

In Fig. C1 top panel, the simulation parameters are defined as follows: $\rho = 10$, yielding a total simulation

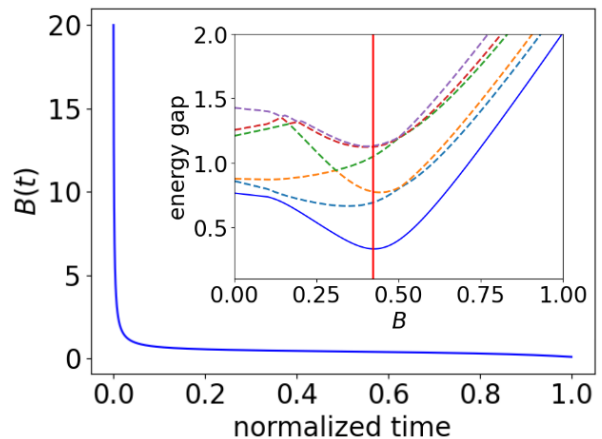


FIG. B1. The local adiabatic field for an 12-site lattice starting from $B_{\max} = 20$ to $B_{\min} = 0.1$ (the same as in Fig. 1). Inset: the blue solid line represents $\Delta(B)$, illustrating the energy gap as a function of the magnetic field for the first coupled excited state. The dashed lines are for higher coupled excited states (not all excited states are shown here). The vertical red line marks the critical magnetic field with the minimum energy gap.

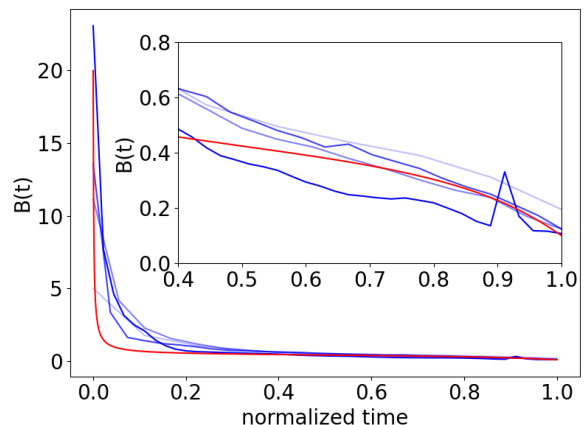


FIG. B2. Optimal $B(t)$ for a 12-site lattice with varying numbers of steps N : 10, 19, 28, 46. The darker the line, the higher the layer count. The inset shows later times for the optimal $B(t)$.

time $t_f = 29.36$. The initial magnetic field $B(t)$ is set to $B_0 = 10$, with a time step $dt = 0.01$. The system is initialized in the ground state of \hat{H}_B . However, since this state is not the true ground state at $B_0 = 10$, this setup introduces diabatic excitations from the start. In this configuration, we observe returns in the instantaneous fidelity, prompting an investigation into whether adiabatic evolution alone can account for this behavior. This is particularly intriguing because local adiabatic evolution typically introduces diabatic excitations at each step without mechanisms to eliminate them, yet such returns are observed here.

To further explore this, we present an additional case,

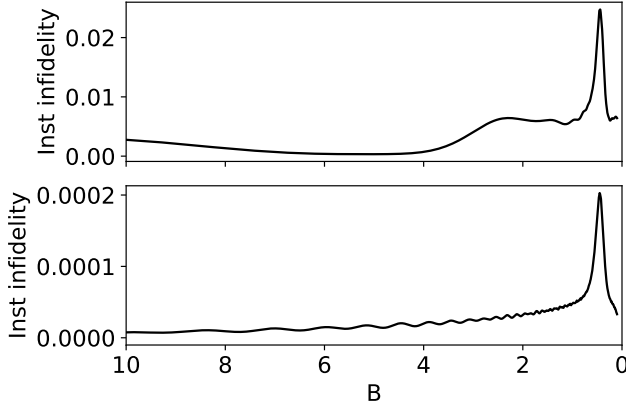


FIG. C1. Instantaneous ground state infidelity during two local adiabatic ramp evolutions. The top panel corresponds to the configuration used in Fig. 1, while the bottom panel represents a more adiabatic-like setting.

shown in the bottom panel of Fig. C1, under modified parameters: $\rho = 100$, resulting in a total simulation time $t_f = 293.7$. The initial magnetic field $B(t)$ is set to $B_0 = 50$, with a smaller time step $dt = 0.001$. The system is initialized in the ground state of $\hat{H}_A + B_0 \cdot \hat{H}_B$, ensuring an initial state with virtually no diabatic excitations, as required by the adiabatic assumption. In this case, the same return pattern in the instantaneous ground state fidelity is observed, but with an amplitude smaller by a factor of 100.

Appendix D: Trotterization of modulated time evolution

In Eq. (7), we show the Trotter formula that translates the modulated time evolution form to a QAOA form. This requires us to approximate a single step in the modulated time evolution by m Trotter steps for the QAOA form.

We begin with the Hadamard lemma,

$$e^{\hat{A}} \hat{B} e^{-\hat{A}} \approx \hat{B} + [\hat{A}, \hat{B}] + \frac{1}{2} [\hat{A}, [\hat{A}, \hat{B}]] + \dots, \quad (\text{D1})$$

and apply it to the expression

$$e^{i\frac{\gamma}{2m}\hat{H}_A} \left(e^{-i\frac{\gamma}{m}\hat{H}_A} e^{-i\frac{\beta}{m}\hat{H}_B} \right)^m e^{-i\frac{\gamma}{2m}\hat{H}_A}, \quad (\text{D2})$$

with $\hat{A} = i\frac{\gamma}{2m}\hat{H}_A$ and \hat{B} the operator inside the parenthesis. We use the QAOA notation of γ and β multiplying the problem and mixer Hamiltonians.

Because of the similarity transformation, the outermost exponential factor goes into the powers inside the parenthesis and then into the argument of the function

inside the parenthesis, so we need to evaluate

$$\left(e^{-i\frac{\gamma}{m}\hat{H}_A} \exp \left[e^{i\frac{\gamma}{2m}\hat{H}_A} \left(-i\frac{\beta}{m}\hat{H}_B \right) e^{-i\frac{\gamma}{2m}\hat{H}_A} \right] \right)^m, \quad (\text{D3})$$

with the Hadamard lemma. Note that this acts only on the operator \hat{H}_B because \hat{H}_A commutes with itself. Expanding the Hadamard lemma out to second order gives us

$$\left(e^{-i\frac{\gamma}{m}\hat{H}_A} \exp \left\{ -i\frac{\beta}{m}(\hat{H}_B + i\frac{\gamma}{2m}[\hat{H}_A, \hat{H}_B]) - \frac{\gamma^2}{8m^2}[\hat{H}_A, [\hat{H}_A, \hat{H}_B]] + \dots \right\} \right)^m. \quad (\text{D4})$$

Next, we use the Baker-Campbell-Hausdorff formula

$$e^{\hat{A}} e^{\hat{B}} = e^{\hat{A} + \hat{B} + \frac{1}{2}[\hat{A}, \hat{B}] + \frac{1}{12}[\hat{A}, [\hat{A}, \hat{B}]] + \frac{1}{12}[\hat{B}, [\hat{B}, \hat{A}]] + \dots}, \quad (\text{D5})$$

for each factor inside the parenthesis to put all terms into one exponent. Here we have

$$\hat{A} = -\frac{i\gamma}{m}\hat{H}_A, \quad (\text{D6})$$

and

$$\hat{B} = -i\frac{\beta}{m} \left(\hat{H}_B + i\frac{\gamma}{2m}[\hat{H}_A, \hat{H}_B] - \frac{\gamma^2}{8m^2}[\hat{H}_A, [\hat{H}_A, \hat{H}_B]] \right), \quad (\text{D7})$$

and we keep only the terms up to two-fold nested commutators. This gives

$$\left(\exp \left\{ -\frac{i}{m}(\gamma\hat{H}_A + \beta\hat{H}_B) - \frac{i\beta\gamma^2}{24m^3}[\hat{H}_A, [\hat{H}_A, \hat{H}_B]] + \frac{i\beta^2\gamma}{12m^3}[\hat{H}_B, [\hat{H}_B, \hat{H}_A]] \right\} \right)^m. \quad (\text{D8})$$

Note how the first order commutator terms cancel out, leaving just the second order nested commutator terms, which come in with an additional power of m in the denominator. This is the advantage of using this form. Because all of the terms in the exponent are now the same, taking the m^{th} power just requires us to multiply the exponent by m , to give

$$\exp \left\{ -i\gamma\hat{H}_A - i\beta\hat{H}_B - \frac{i\beta\gamma^2}{24m^2}[\hat{H}_A, [\hat{H}_A, \hat{H}_B]] + \frac{i\beta^2\gamma}{12m^2}[\hat{H}_B, [\hat{H}_B, \hat{H}_A]] \right\}. \quad (\text{D9})$$

Hence, the error of this form is of order $1/m^2$.

We define an error ratio ζ to be

$$\zeta = \max \left(\frac{\left| \frac{\gamma^2\beta}{24m^2} \right|}{|\gamma| + |\beta|}, \frac{\left| \frac{\gamma\beta^2}{12m^2} \right|}{|\gamma| + |\beta|} \right). \quad (\text{D10})$$

This parameter determines the value of m needed to ensure that the energy difference before and after Trot-

terization is within 30%. Unlike other works that provide full Trotter error analysis [51, 52], this error ratio serves only as a relative indicator.